RSC Advances

RSC Advances

www.rsc.org/advances

ROYAL SOCIETY OF CHEMISTRY

www.rsc.org/advances

RSC Advances

ARTICLE

Facile Green Synthesis of Palladium Quantum Dots@Carbon on Mixed Valence Cerium Oxide/Graphene Hybrid Nanostructured Bifunctional Catalyst For Electrocatalysis of Alcohol and Water

Ramanujam Kannan[a,b], Hye-Ri Jang[b], Eun-Sil Yoo[b] , Hong-Ki Lee[c], Dong Jin Yoo[a,b*]

Abstract

The development of an efficient catalyst for proton exchange membrane fuel cells is presently a challenging and pressing need. Enhanced activity is expected to occur if the interactions between the catalytic metal and the support are improved. Herein, we report the eco-friendly green solid state synthesis of palladium quantum dots@carbon on mixed valence cerium oxide nanoparticles/reduced graphene oxide hybrid (PdQD@C-CeOx/RGO) nanocomposites. We also detail their notable performance in the electrocatalysis of ethylene glycol and water in alkaline medium. The palladium nanoparticles, which are 2-5 nm in size, are formed in a fast manner. In terms of catalytic activity, the low-quantity palladium nanoparticle (5 wt%)@carbon-cerium oxide/reduced graphene oxide on the electrode exhibit the highest forward anodic peak current density (10 mA/cm^2) compared with the Pd/CeOx and Pd/RGO nanocomposite electrodes. The cerium oxide/reduced graphene oxide functions as both the support and in assisting the electrooxidation reactions towards removal poisonous intermediates formed during the electrooxidation of ethylene glycol. This work could provide new insights into the simple fabrication of high-performance catalytic electrodes for fuel cell applications.

1. Introduction

Future hydrogen-based sustainable energy systems are mainly focused on energy efficient fuel cell technologies. In particular, low temperature, direct alcohol fuel cells have been widely accepted as an easy and energy efficient energy provider for room temperature, small to medium power requirements [1-5]. Various alcohols have been used as liquid fuels, including methanol [6], ethanol [7], ethylene glycol [8], etc. These have been studied by many researchers because they are able to provide high power output and easy storage/handling compared to pure hydrogen [1-8]. Over the past few decades, direct methanol fuel cells have been widely studied and considered as a possible power source for portable electronics [6]. However, methanol has some disadvantages, such as toxicity, flammability, a low boiling point, and, due to its smaller size, methanol crossover from the anode to the cathode can result in a marked decrease in the efficiency of the system [7-10].

As a result, attempts have been made to find an alternative to methanol. Ethylene glycol (EG) has been suggested as an alternative energy carrier for fuel cells due to its high energy density, higher boiling point, low vapour pressure, non-toxicity, extensive availability from renewable sources, and its relatively effortless transport and storage [11,12].

Recently, nanostructured metal catalysts have found extensive application in fuel cell electrocatalysis. The development of an active electrocatalytic system is challenging. Recent studies have found that platinum (Pt) is one of most effective catalysts for direct alcohol fuel cells (DAFCs) [13-15]. However, platinum's high cost, limited availability, and propensity to generate intermediate

poisonous compounds during the electrooxidation process represent serious drawbacks. Therefore, reducing the dependence on Pt by developing a Pt-free catalyst would likely be advantageous. Palladium (Pd) and Pd-based catalysts have been considered as suitable catalysts for DAFCs and could be used as a potential substitute for Pt. In addition, Pd is comparatively inexpensive and more abundant compared to Pt. Pd and Pt also exhibit almost identical electrocatalytic performance towards DAFCs [13-16].

Supported metal catalysts exhibit enhanced catalytic activity and stability compared to unsupported catalyst. Typically, the support material provides an improved physical surface for the metal catalyst, resulting in an improved surface area that allows for the maximum number of catalytic centres to be available for the reaction [17-20]. Traditionally, different types of conductive carbon black (Vulcan XC, Ketjen Black, and Denka Black) have been used as the support material for noble metals in electrochemical reactions [4, 20]. To improve the electrical conductivity and surface area, carbon nanotubes, carbon nanofibers, and graphene have been used as support materials [4, 15,20,21].

Graphene is a thin, nanostructured material with sp^2-hybridized carbon atoms arranged in a honeycomb lattice. Recently, graphene-based materials have attracted considerable attention in energy fields due to their multitude of beneficial properties such as high surface area, high electrical conductivity, and good thermal and mechanical stability. These unique properties have facilitated the use of graphene in energy storage and conversion applications. In the recent past, graphene-based materials have been used as the support material for precious metal nanoparticles in the fields of energy conversion (especially for fuel cell electrocatalysis) [4, 20,21].

Consequently, efforts were made to develop size-confined metal nanoparticles/graphene composites for electrocatalytic energy conversion and biosensing applications [21-24].

Additionally, metal oxides are considered to be an emerging catalytic support material for PEMFCs. Due to their high surface area, high thermal and mechanical stabilities, easy synthesis, and their ability to be converted into any form, these materials are very versatile. Some metal oxides, such as TiO_2, MnO_2, SnO_2, NiO, CeO_2, etc., have been tested as support materials for DAFCs [18-20,24-27]. However, these metal oxides suffer from lower conductivities, which cause the overall energy output to decrease. To overcome this shortcoming, these metal oxides have been composited with carbon materials such as carbon black [24,25], carbon nanotubes [28,29], graphene oxide [28-30], etc., in order to develop supports that will help to synergistically enhance DAFC performance [30-41]. Additionally, the strong interaction between the metal catalyst and the support plays a significant role in electrode performance [4, 20, 24, 30,31].

With this in mind, we have attempted to synthesize graphene oxide/ceria supported palladium quantum dots@carbon hybrid nanostructures for the efficient electrocatalyst of ethylene glycol oxidation. With the aim to provide active oxygen species to the catalyst, ceria has been chosen as an additional support. In addition, this facile approach improves the interaction between the catalytic metal and the support by developing in situ carbon. The influence of the support material (graphene oxide/ceria) and the in situ generated carbon on the electrooxidation of ethylene glycol and water electrolysis are studied in an attempt to reduce the noble metal content while simultaneously maximizing catalytic performance.

2. Results and discussion

2.1. Physical characterization of the PdQDs@C-CeOx/RGO hybrid nanostructures

Figure 1 shows the powder XRD patterns of the CeOx, GO, PdQDs-CeOx/RGO, and PdQDs@C-CeOx/RGO hybrid nanostructures. The samples reveal peaks at 28.6, 33.0, 47.4, and 56.6° 2θ , which correspond to the (111), (200), (220), and (311) planes of the cubic fluorite structure of the cerium oxide (CeO_2) nanoparticles, respectively, as identified using JCPDS 89-8436. In addition, the peak at 29.2° 2θ indicates the formation of Ce_2O_3. The prepared cerium oxide is pale yellow in colour, although pure CeO_2 is colourless [12]. From these results, the prepared material is determined to be a mixed valance ceria, i.e., a combination of CeO_2 and Ce_2O_3. Hence, we refer this material as CeOx. The XRD peak at 10.3°, 2θ corresponds to the C(002) for GO (Figure 1b) and the Pd-CeOx/RGO material shows two significant peaks for CeOx (111) and Pd (200) with slight shift in peak position and the disappearance of peak at 10.3 and presence of broad peak around 20-23°, indicates the reduction of GO and turned into RGO (Figure 1c). As seen from Figure 1d, the peaks at 39.9 (111) and 45.2° 2θ (200) indicate the presence of Pd QDs on the CeOx/RGO support. The slight shift in peak position [from Pd peaks of 40.1 (111) and 45.6° 2θ (200); JCPDS 88-2335] indicates the formation the Pd@C nanostructures [24, 42]. The formation of carbon is derived from the reductant (i.e., ascorbic acid).

The generation of Pd QDs over the support was achieved by an eco-friendly, solid state method using ascorbic acid (AA) as the reducing agent. AA is beneficial compared to common reducing agents, such as borohydride, hydrazine, etc., because these reducing agents are not environmentally-friendly and reactions with these reductants can be very fast or uncontrollable. Conversely, AA is a mild reducing agent and its reactions can be easily controlled. In addition, the oxidized and/or unoxidized reductant serves as the

carbon source; these carbon supports are expected to enhance the interaction between the metal catalyst and the support material. The improved metal catalyst and support yield enhanced mass transfer and maximize the catalytic utilization [24,31].
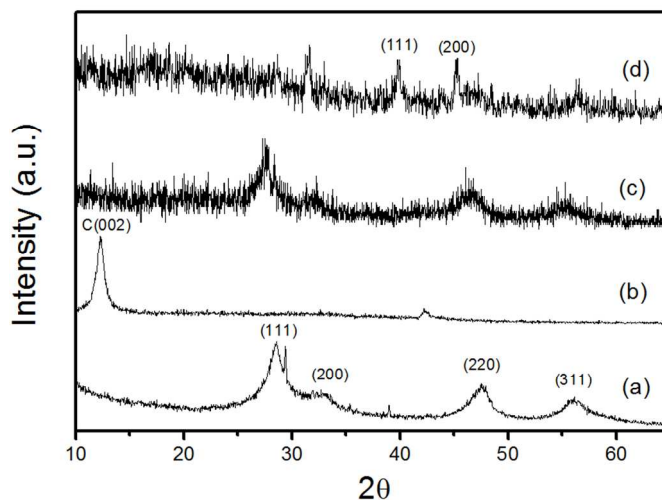

Fig.1. Powder X-Ray diffraction spectra of (a) CeOx, (b) GO, (c) Pd QDs-CeOx/RGO, and (d) PdQDs@C-CeOx/RGO hybrid nanostructures
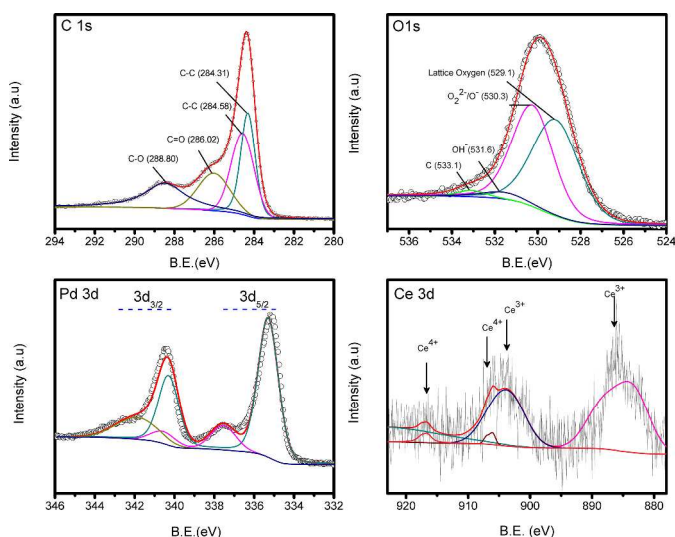

Fig.2. Deconvoluted X-ray photoelectron spectra of PdQDs@C-CeOx/RGO hybrid nanostructures

X-Ray photoelectron spectra analyses were carried out to investigate the surface chemical states of C, O, Ce, and Pd species in the PdQDs@C-CeOx/RGO hybrid catalyst. Figure 2 shows the deconvoluted C1s XPS spectrum of the PdQDs@C-CeOx/RGO hybrid, in which the peak at the binding energy of C1s is observed at ca. 284.4 eV. This feature can be further separated into four peaks at 284.31, 284.58, 286.02, and 288.80 eV, which correspond to C-C/C=C, C-C, C=O, and C-O, respectively. The PdQDs@C-CeOx/RGO exhibits two major peaks at 335.5 eV (Pd3d$_{5/2}$) and 340.5 eV (Pd3d$_{3/2}$), indicating the formation of metallic Pd nanoparticles. The deconvoluted O1s spectrum exhibits peaks at 529.1 eV, 530.3 eV, and 531.6 eV, corresponding to lattice oxygen, O_2^{2-} /O^-, and OH^- of the CeOx material. In addition, a peak at 533.1 eV is also observed [24, 42, 43], which indicates that the carbon material is formed/derived from an organic precursor (i.e., ascorbic acid). The deconvoluted Ce3d core-level spectrum is

presented in Figure 2. Major peaks were observed at 917.2 and 906.8 eV, corresponding to Ce (IV). Ce (III) also exhibits features at 904.2 eV, 886.2 eV, and some other less intense peaks. Because the Ce3d level signals come from a very complicated satellite structure, their definite bands have yet to be concluded [39]. The wide range of XPS profiles shown in this study make it clear that the Ce^{4+} and Ce^{3+} oxidation states exist in the PdQDs@C-CeOx/RGO hybrid catalyst.

Figure 3 shows the Raman spectra of (a) RGO, (b) CeOx/RGO, and (c) PdQDs@C-CeOx/RGO hybrid nanostructures.

The Raman spectra of the RGO (Figure 3a) exhibits two characteristic peaks at 1359 cm^{-1} and 1593 cm^{-1}, which correspond to D and G bands, respectively. These peaks have an intensity ratio (I_D/I_G) of 0.9901 [24]. The CeOx/RGO exhibits three peaks at 454 cm^{-1}, 1359 cm^{-1}, and 1593 cm^{-1}, which match with the CeOx, D, and G bands of RGO, respectively (Figure 3b). The main peak at 454 cm^{-1} is attributed to the F_{2g} vibrational mode of CeOx, which is the Raman active mode of CeOx. In general, the defect free (single crystal) CeO_2 exhibits a Raman band at 466 cm^{-1} [44,45]. However, the CeOx/RGO shows a peak at 454 cm^{-1} instead of at 466 cm^{-1}. This shift is attributed to the occurrence of defects and the smaller particle size of CeOx. Additionally, as can be seen from the PdQDs@C-CeOx/RGO Raman spectra shows a peak at 610 cm^{-1} (Figure 3c), attributes to the internsic oxygen vacancies of the CeOx. The reduced intensity of the CeOx Raman band is associated with reduced particle size of CeOx and the increased D band (RGO) intensity than G band, is , presumed to the formation of carbon materials over the CeOx/RGO. This was further confirmed the Raman spectra for Pd over CeOx/RGO heated before and after microwave heating (Fig. S3), the sample before microwave irradiation shows higher G band than D band, on the other hand after heating the I_D is comparatively higher the I_G indicates the formation of carbonous material [24].
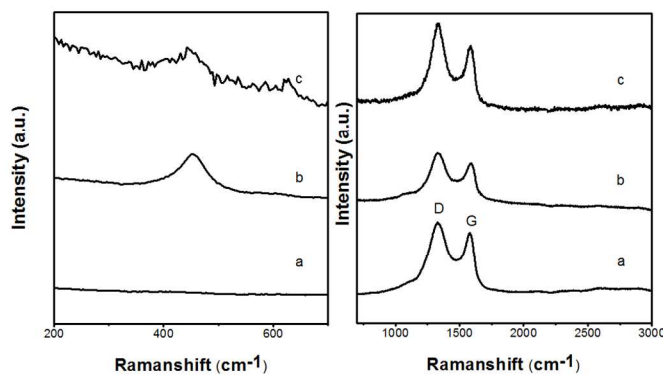

Fig. 3. Raman spectra of (a) RGO, (b) RGO/CeOx, and (c) Pd QDs@C-CeOx/RGO hybrid nanostructures.

The surface morphologies of the prepared materials were analysed by transmission electron microscopy (TEM). As seen in Figure 4a, the few layers of the graphene sheets were clearly observed. As seen from Figure 4b, the CeOx particles formed like oval shaped particles on the graphene sheets. The CeOx particle size about 20 nm. Pure CeOx exhibits an almost identical morphology (Figure S4). The high resolution TEM images show (Figure 4d &e) that the PdQDs with black coloured spherical shaped and CeOx nanoparticles are also spherical morphology with the particle size of about 10 nm were uniformly distributed over the RGO. In addition to that the fringes patterns of CeOx nanoparticles are also shown clearly in Fig. 4e. The particle size of the PdQDs ranges between 2 and 5 nm (Figure 4f). This clearly indicates that AA effectively reduced both the Pd and CeOx. As-prepared

PdQDs@C-CeOx/RGO was further analysed by high-angle annular dark-field (HAADF) imaging using a scanning transmission electron microscope (STEM) equipped with an energy dispersive X-ray analyser. The HAADF-STEM image shows (Fig. S5) the wide distribution of Pd and CeOx nanoparticles over the graphene sheets. The line scan indicates that the Pd and CeOx catalyst QDs are present individually as well as present in the arrangement where the Pd QDs are over the CeOx (Fig. S5).
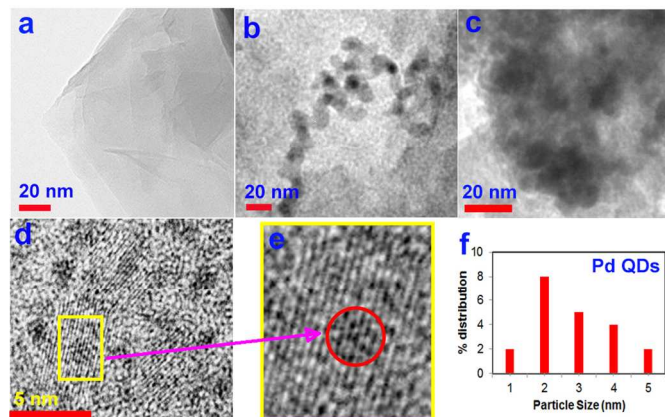

Fig. 4. TEM of (a) RGO, (b) RGO/CeOx, (c) PdQDs@C-CeOx/RGO hybrid nanostructures. (d) High resolution transmission electron micrograph, (e) fringe patterns of PdQDs@C-CeOx/RGO hybrid nanostructures, (f) particle size distribution of Pd QDs.
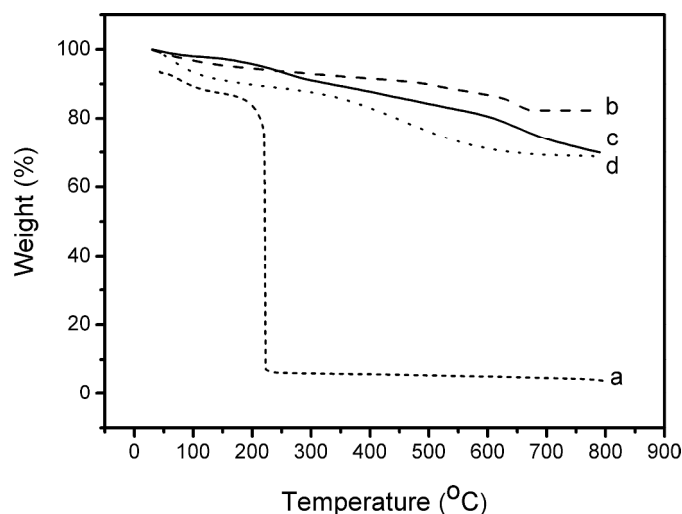

Fig.5. Thermogravimetric profile for (a) GO, (b) CeOx, (c) Pd-CeOx/RGO, and (d) PdQDs@C-CeOx/RGO

The stability of the PdQDs@C-CeOx/RGO catalyst was analysed by thermogravimetric analysis (TGA) between room temperature and 800 °C under a nitrogen atmosphere. As seen from Figure 5a, the GO exhibits a major weight loss between 100 and 200 °C, indicating the removal of the oxygen-containing functional groups present in the GO. Another major weight loss, of about 90%, occurred at 220 °C, indicating that more oxygen-containing functional groups were removed [46]. The TGA curve for CeOx shows that the material is highly stable until a significant transformation in the structure was observed at 700 °C. A significant difference was observed between the Pd-CeOx/RGO (Figure 5c) and PdQDs@C-CeOx/RGO nanostructures (Figure 5d), although both materials do exhibit surface and layered oxygen losses around 200 °C. The Pd-CeOx/RGO exhibits an additional

weight loss around 300 °C, indicating the removal of organic materials. This suggests that the oxidized/unoxidized AA is eliminated at this point. Alternatively, the PdQDs@C-CeO$_X$/RGO material shows a major weight loss around 450 °C, indicating the presence of carbon in the catalyst. This improved thermal stability is due to the presence of the Pd and CeOx nanoparticles. The higher weight loss of Pd QDs @C-CeOx/RGO is presumed to be caused by the presence of the carbon materials, which formed over the catalyst, and begin to degrade around 400 °C. The content of the carbon material is higher in the PdQDs@C-CeOx/RGO compared to the Pd-CeOx/RGO.

2.2. Electrocatalysis of EG on the PdQDs@C-CeOx/RGO hybrid nanostructure

The voltammetric behaviour of Pd/C-, Pd/CeOx-, Pd/RGO-, and PdQDs@C-CeOx/RGO-modified glassy carbon electrodes under the same conditions was tested. As shown in Fig. 6A, the cyclic voltammograms (CVs) of (a) Pd/C, (b) Pd/CeOx, (c) Pd/RGO, (d) Pd-CeOx/RGO, and (e) PdQDs@C-CeOx/RGO electrodes in 1 M KOH were recorded at a scan rate of 25 mV/s in the potential range between -1.1 and +0.2 V. In general, Pd in an alkaline electrolytic medium exhibits four significant peaks, which can be observed during sweeping: surface adsorbed hydrogen oxidation (*pI*), hydroxyl adsorption over the electrode (*pII*), Pd oxidation (*pIII*), and Pd reduction (*pIV*). As seen from the voltammograms, which compare the Pd/C, Pd/CeOx, Pd/RGO, and Pd-CeOx/RGO modified electrodes, the PdQDs@C-CeOx/RGO electrode exhibits a higher peak current response. This is attributed to the smaller size of the Pd/CeOx nanoparticles and to the fact that carbon enhances electron transport, resulting in more active sites for the reaction. The RGO acts as good platform the Pd QDs; thus, the Pd oxidation peak in this material was higher than either the Pd/CeOx or Pd/C. Figure 6A (e) shows the improved CV response, indicating that the availability of active Pd sites was improved by the addition of CeOx in the RGO. Additionally, a greater number of active catalytic sites are achieved after microwave irradiation, i.e., the in situ generated carbon helps to improve the interaction between the support and the catalyst. From these results, we conclude that both the CeOx and the carbon help to achieve an improved voltammetric response. Further voltammetric studies were performed for the ethylene glycol electrooxidation reaction at the PdQDs@C-CeOx/RGO electrode.

Figure 6B shows the CVs of electrooxidation of 0.5 M EG in a 1 M KOH solution on the PdQDs@C-CeOx/RGO hybrid catalytic electrode in the scan range between -1.1 V and +0.2 V (vs SCE). The EG electrooxidation promoted by the PdQDs@C-CeOx/RGO is characterized by two well-defined peaks, which are observed during the forward and backward scans. These peaks are attributed to the electrooxidation of EG (during the forward scan, O^f) and the re-oxidation of the intermediates formed during the forward sweep (during the reverse scan, O^b). For comparison, the Pd/C, Pd/RGO, Pd/CeOx, and Pd/CeOx/RGO electrodes were tested for their EG electrooxidation.

These results indicated that the PdQDs@C-CeOx/RGO electrode exhibited the highest activity. The degree of EG electrooxidation at various electrodes was analysed by the forward (I_f) and backward (I_b) peak current density ratios. The I_f and I_f/I_b of the Pd-RGO/CeOx is much higher than those of the Pd/C, Pd/RGO, Pd/CeOx, and Pd/CeOx/RGO catalysts (Table 1). This indicates that the electrocatalytic activity of the PdQDs@C-CeOx/ RGO is clearly higher than those of the other electrodes.
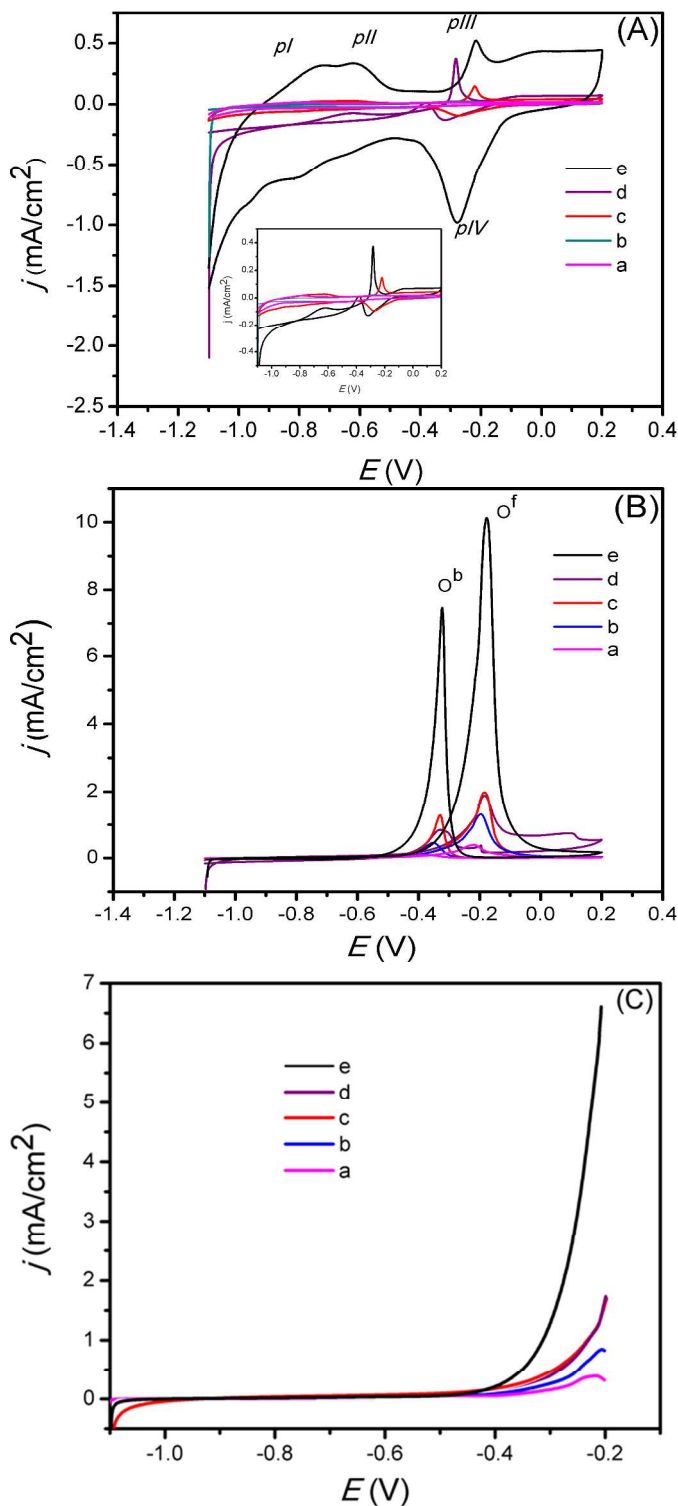

Fig.6. CVs for the electrochemical characteristics of (a) Pd/C, (b) Pd/CeOx, (c) Pd/RGO, (d) Pd-CeOx/RGO, and (e) Pd@C-CeOx/RGO electrodes in (A) 1 M KOH and (B) 0.5 M EG + 1 M KOH; (C) onset potential for the electrooxidation of EG on of (a) Pd/C, (b) Pd/CeOx, (c) Pd/RGO, (d) Pd-CeOx/RGO, and (e) PdQDs@C-CeOx/RGO electrodes.

Table 1

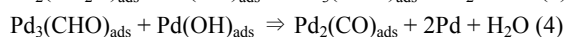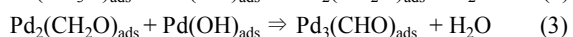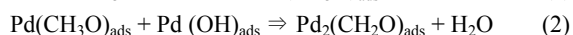|	PdQDs@C-CeOx/RGO	Pd-CeOx/RGO	Pd/C	Pd/RGO	Pd/CeOx
ESA (m^2/g)	182.61	37.07	15.80	34.07	7.90
I_f (mA/cm^2)	9.80	1.0	0.40	2.02	1.52
I_f/I_b	1.42	1.31	1.33	1.36	1.33

*average Pd loading on the catalyst is 0.2 mg

A good catalyst exhibits a lower onset potential of the electrooxidation reaction and plays a significant role in accessing electrocatalytic activity. The onset potential can be estimated by looking at the potential at which the deviation from the baseline occurs in the forward oxidation peak. As seen in Figure 6C, the electrocatalytic reaction at PdQDs@C-CeOx/RGO starts at -055 V, .which is a comparatively lower onset potential compared to the other electrodes, indicates the presence of a greater number of available active sites on the electrode surface. This causes more fuel/electrolyte to approach the electrode surface, facilitating the electrocatalytic reaction

2.3. Water electrolysis reaction and possible removal of poisonous intermediates

The Hydrogen and oxygen generation through water electrolysis find important in the present scenario to develop a green energy source. The water electrolysis efficiency is limited by the large anodic over overpotential of the oxygen evolution process. Water electrolysis i.e., the generation of active oxygen atoms at anode was studied at the Pd QDs@C-CeOx/RGO electrode (Figure 7A). CV of the Pd QDs@C-CeOx/RGO electrode in a 1 M KOH solution, with the potential at (E_{upper}) +1.0 V, shows that the OER starts much earlier i.e., +0.12 V and the maximum number of oxygen atoms was generated at the higher potential (+1. 0V) and that the corresponding oxygen reduction reaction is observed at -0.53 V. The Pd QDs@C-CeOx/RGO exhibits a higher OER and a higher oxygen reduction reaction current compared with the Pd-C, Pd-CeOx, Pd/RGO, Pd-CeOx/RGO, and PdQDs@C-CeOx/RGO electrodes. This indicates that in situ generated carbon has marked effect on the electrocatalytic reaction, in addition to that the RGO/CeOx acts as co-catalyst for the Pd and helps to extract active oxygen atoms from the electrolyte.

It is generally accepted that the electrooxidation of alcohols can be poisoned by intermediates [M(CO)$_{ads}$] that are produced during the forward scan (equation 1-4), which suppress electrocatalytic activity [2,3]. To overcome this, we extended the E_{upper} range, step by step, from +0.2 V to +1.0 V. This resulted in a gradual decrease in I_b and no change in I_f. At the higher scanning range (+1.0 V), an insignificant I_b was noticed. In addition, a new oxidation peak was observed at +0.5 V (O^{f2}). This lowered I_b and O^{f2} indicate that the intermediates were oxidized during the forward sweep itself (Figure 7 B).

$$2\,Pd + CH_3OH \Rightarrow Pd(CH_3O)_{ads} + PdH \qquad (1)$$

$$Pd(CH_3O)_{ads} + Pd\,(OH)_{ads} \Rightarrow Pd_2(CH_2O)_{ads} + H_2O \qquad (2)$$

$$Pd_2(CH_2O)_{ads} + Pd(OH)_{ads} \Rightarrow Pd_3(CHO)_{ads} + H_2O \qquad (3)$$

$$Pd_3(CHO)_{ads} + Pd(OH)_{ads} \Rightarrow Pd_2(CO)_{ads} + 2Pd + H_2O \quad (4)$$

The oxidation of this strongly bonded intermediate species requires highly active oxygen atoms. Such oxygen atoms may not be available until E_{upper} = +0.2 V.
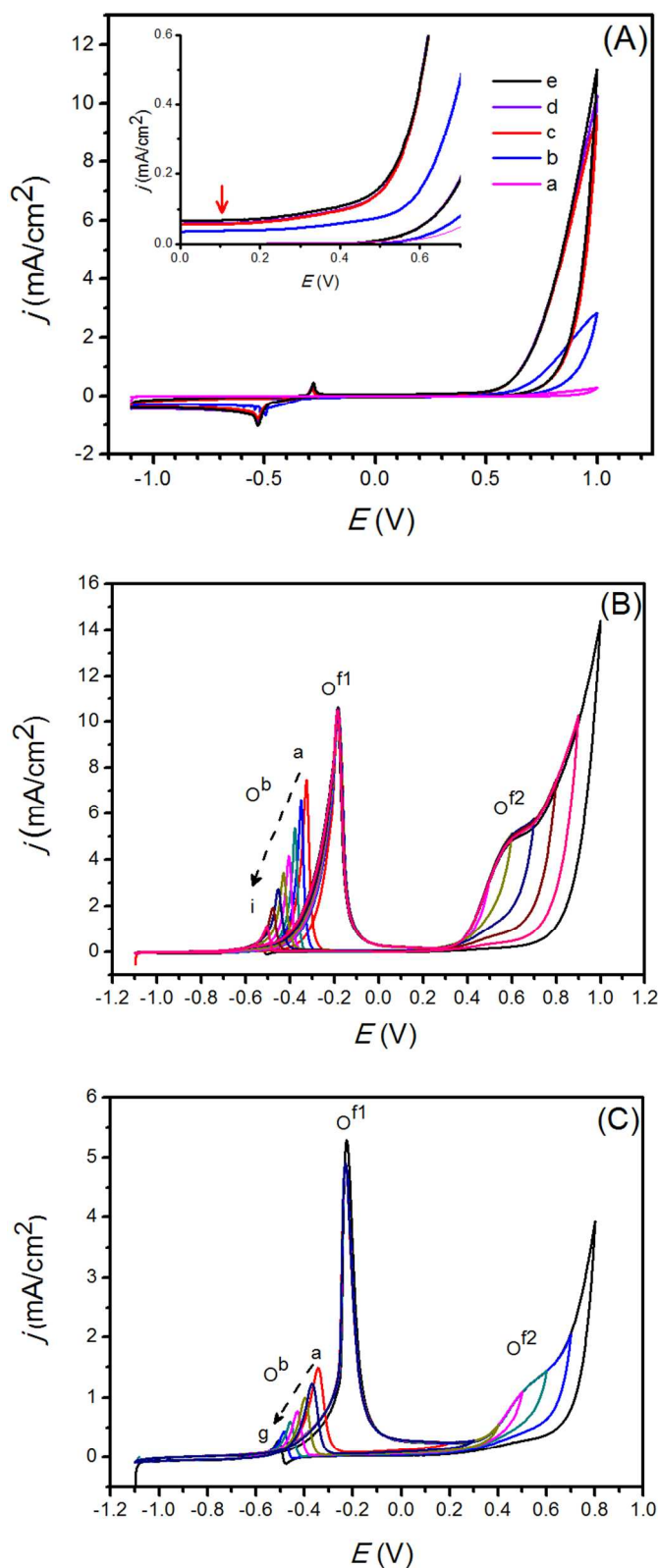

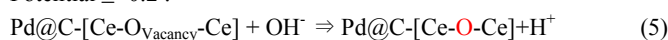Fig.7. CVs for the electrooxidation of (A) Water electrolysis reaction (oxygen evolution reaction) at (a) Pd/C, (b) Pd/CeOx, (c) Pd/RGO, (d) Pd-CeOx/RGO, and (e) PdQDs@C-CeOx/RGO electrodes in 1 M KOH solution. (B) EG (0.5 M) and (C) CH$_3$OH (0.5 M) at PdQDs@C-CeOx/RGO at various applied potentials [E_{upper} from (a-i) +0.2 V to +1.0 V] in a 1 M KOH solution.

RSC Advances Accepted Manuscript

As the E_{upper} is increased, highly active oxygen atoms become available and gradually oxidize the intermediate species As the E_{upper} is gradually increased above +0.2 V, the catalytic support (CeOx) generates active oxygen; the concentration of active oxygen is directly associated with the E_{upper}. This active oxygen will help to oxidize the intermediates formed throughout the course of EG electrooxidation.
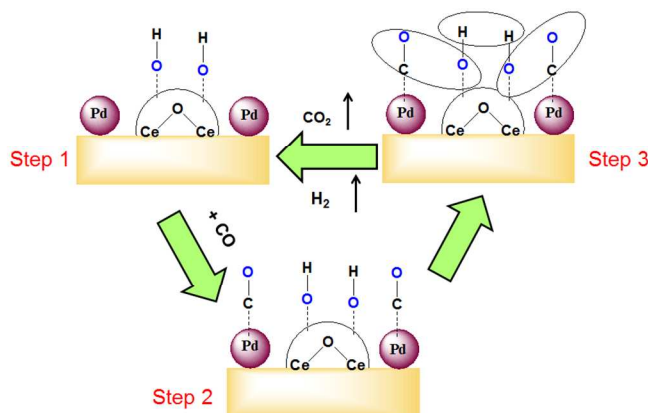
The maximum potential at which the oxygen evolution reaction (OER) occurs is +1.0 V. This results in the effective oxidation of the intermediates that form on the electrode surface. The enhanced active oxygen generation results from the combined effects of RGO/CeOx. In addition, CeOx is prepared by a low temperature method, so it is enriched with surface oxygen that contains more surface defects. At higher potentials, the CeOx combines with the hydroxyl to generate active oxygen, which is highly energetic and subsequently oxidize the intermediates on the electrode surface (Equation 5&6).

For methanol oxidation, similar activity was observed (Figure 7C). We have tested methanol oxidation at higher potentials; the backward oxidation current decreased progressively and the maximum reduction of the poisonous intermediates became oxidized when the E_{upper} reached + 0.8 V. Above this potential (Eupper = +0.8 V), PdO formation was higher (confirmed by the observation of an oxygen reduction peak).

Potential ≤+0.2 :

$$Pd@C-[Ce-O_{Vacancy}-Ce] + OH^- \Rightarrow Pd@C-[Ce-O-Ce]+H^+ \quad (5)$$

Potential ≥+0.2:

$$Pd@C-[Ce-O-Ce]+OH^- \Rightarrow Pd@C-[Ce-O_{Vacancy}-Ce]+[O]_{active} +H_2O \quad (6)$$

Scheme 1: Reaction sketch for the synergism of CeOx during the oxidation of intermediates on the Pd QDs surface

By comparing these results with Pd/RGO (for E_{upper} = +0.6 V), the O^b peak current is seen to decrease significantly (Fig.S6). Alternatively, when the E_{upper} > 0.6 V, a drastic reduction of the O^f peak current was observed. It indicates that the gradually above the forward oxidation current reduced significantly This indicates that the electrode is inactive. We presumed that at higher potentials Pd oxidized into PdO. These oxidized species are less catalytically active than the unoxidized Pd. Therefore, the electrocatalytic activity was reduced/suppressed. From these results, it is clear that the CeOx plays a significant role and acts synergistically enhance the activity of the catalyst. The possible reaction that occurs on the PdQDs@C-RGO/CeOx electrode surface is given by Scheme 1.

The electrooxidation of methanol and ethylene glycol exhibit similar electrochemical activities. These results indicate that an improved electrocatalytic activity for ethylene glycol oxidation was achieved by using the RGO/CeOx. The RGO/CeOx acts as both the support as well as the co-catalyst and act as bifunctional catalyst. The present solid state method for grafting noble metals onto the support material represents a new, fast way to develop nanocatalysts with improved electrocatalytic performance. The in situ generated carbon will help to enhance the interaction between the catalyst and the support. Additionally, supported ternary nanocatalysts exhibit improved catalytic activity with small quantities of noble metals (5 wt% Pd); in this way, the cost of the catalyst can be reduced. The present work is expected to provide a simple and novel way to produce metallic QDs and improve interaction with the support. These materials have the potential to be utilized extensively in energy (fuel cell) applications

3. Experimental

3.1. Materials

Natural graphite powder, sodium borohydride, potassium permanganate, and cerium nitrate were purchased from Alfa Aesar Chemicals. Palladium chloride, methanol, ethanol, ethylene glycol, and 4-nitrophenol were obtained from Sigma-Aldrich Chemicals. Ascorbic acid (Daejung Chemicals), sulphuric acid, and nitric acid were received from Samchun Pure Chemicals. All of the reagents were used as-received without further purification. Double–distilled deionized water was used throughout the study.

3. 2. Synthesis of ceria and graphene/ceria composite

Graphene oxide (GO) were synthesized using the modified Hummers' method [31, 24]. The CeOx/GO nanocomposite support was prepared as follows: about 10 mg of GO and 5 mL of 0.1 M of cerium nitrate were dispersed in 40 mL of deionized water and subjected to sonication for 2 h. Then, a 2 M sodium hydroxide solution was added slowly to the cerium nitrate/GO mentioned above. The resultant precipitate was set aside for 24 h. Next, the precipitate was washed with deionized water and dried in a hot air oven at 110 °C for 24 h. The CeOx was also prepared by the method described above, but without the GO.

3.3. Grafting of PdQDs@carbon on the CeOx/RGO composite

The PdQDs@C-CeOx/RGO catalyst was prepared using the solid state and chemical reduction methods. Briefly, about 45 mg of CeOx/RGO and 10 mg of PdCl$_2$ were mixed well in a mortar for 10 min. Then, 10 mg of ascorbic acid was added to the mixture and mixed well in the mortar. After waiting 1 min, until the colour of the solid changed from grey to black colour paste, the mixture was ground for another minute before being subjected to microwave irradiation using a domestic microwave oven for 5 min at regular intervals of 30 s. For comparison, Pd nanoparticles were also dispersed in CeOx, GO, and commercial carbons support (Vulcan XC); these catalysts were prepared in the same manner. The Pd loading in each catalyst was 5 wt%.

3.4. Electrode fabrication

About 1 mg of the PdQDs@C-CeOx/RGO catalyst was dispersed ultrasonically in 0.1 mL of a Nafion (0.05%)/0.9 mL water solution; then, 10 μL of the well-dispersed PdQDs@C-CeOx/RGO catalyst ink was dropped onto the GC electrode surface and vacuum dried at room temperature. The electrochemical studies were performed under nitrogen saturated conditions at room temperature (23±2 °C). These measurements were taken with respect to a standard calomel electrode.

Conclusions

Pd Quantum dots on CeOx/RGO were successfully and quickly (within than 5 min) synthesized by an environmentally-benign method using ascorbic acid. The ascorbic acid served as both the reductant and the stabilizing agent for the Pd QDs. The Pd nanoparticles were uniformly distributed over the RGO/CeOx, and their average particle size was between 2 and 5 nm. A Pd metal content of 5 wt% on the RGO/CeOx showed improved electrochemical performance towards the oxidation of ethylene glycol in an alkaline medium. The PdQDs@C-CeOx/RGO exhibits excellent water electrolysis reaction. By increasing the E_{upper}, the poisoning intermediates were removed through oxygen evolution reactions. This PdQDs@C-CeOx/RGO hybrid nanocomposite can be used as an effective catalyst for direct alcohol fuel cells. The in situ generated carbon improves the interaction between catalyst and support interaction. The proposed method is simple, quick and eco-friendly methods of synthesis of the metal/metal oxide nanoparticle-decorated graphene catalyst have the potential use in the fuel cell electrocatalysis.

Acknowledgements

Notes and References

[a] R&D Education Center for Specialized Graduate School of Hydrogen and Fuel Cells Engineering, [b] Graduate School, Department of Energy Storage/Conversion Engineering, Hydrogen and Fuel Cell Research Center, Chonbuk National University, Jeollabuk–do, 561-756, Korea
Email:djyoo@jbnu.ac.kr
[c]Hydrogen Fuel Cell Parts and Applied Technology Regional Innovation Center, Woosuk University, Jeollabuk-do 565-902, Korea.

1. H. Liu, J. Zhang, Wiley-VCH Verlag GmbH & Co. KGaA,Weinheim, 2009, pp 1–70.
2. M. Li, R.R. Adzic, R. R. *Low-Platinum-Content electrocatalysts for methanol and ethanol electrooxidation in Electrocatalysis in Fuel cells: A Non- and Low- Platinum approach* (Ed. M. Shao), Springer-Verlag, London 2013.
3. H. Zhang, P. K. Shen, *Chem. Rev*. 2012, 112, 2780.
4. H. Huang, X. Wang, *J. Mater. Chem. A* 2014, 2, 6266.
5. G. L. Soloveichik, *Bellstein. J. Nanotechnol*. 2014, 5, 1399.
6. C. Xu, P. K. Shen, *Chem. Comm.* 2004, 2238–2239.
7. A. A. Gutierrez, A. M. Fernandez, F. J. R. Varela, *Int. J. Hydrogen energy* 2013, 38, 12657.
8. E. Antolini, E.R. Gonzalez, *J. Power Sources* 2010, 195, 3431.
9. C. Bianchini, P. K. Shen, *Chem. Rev.* 2009, 109, 4183.
10. R. Kannan, K. Karunakaran, S. Vasanthkumar, *Ionics*, 2012, 18, 803.
11. A. Serov, C. Kwak, *Appl Catal B: Environ*. 2010, 97, 1.
12. C. Jin, Y. Song, Z. Chen, *Electrochim Acta* 2009, 54, 4136.
13. J. Schnaidt, M. Heinen, Z. Jusys, R. J. Behm, *J. Phys. Chem. C* 2013, 117, 12689.
14. J. Schnaidt, M. Heinen, Z. Jusys, R. J. Behm, *J. Phys. Chem. C* 2012, 116, 2872.
15. L. Gao, W. Yu, S. Tao, L. Fan, *Langmuir* 2013, 29, 957.
16. H. You, S. Yang, B. Ding, H. Yang, **Chem. Soc. Rev.** 2013, 42, 2880.
17. C. Xu, Z. Tian, P.K. Shen, S. P. Jiang, *Electrochim. Acta* 2008, 53, 2610.
18. R. Kannan. A. R. Kim, D.J. Yoo, *J. Appl. Electrochem.* 2014, 44, 893.
19. E. H. Yu, U. Krewer, J. Scott, *Energies* 2010, 3, 1499.
20. Y. J. Wang, D. P. Wilkinson, J. Zhang, *Chem. Rev.* 2011, 111, 7625.
21. S. Sharma, B. G. Pollet, *J. Power Sources* 2012, 208, 96.
22. E. Antolini, *Appl. Catal. B. Environ.* 2012, 123-124, 52.
23. G. Z. Hu, F. Nitze, X. Jia, T. Sharifi, H. R. Barzegar, E. G. Espino, T. Wagberg, *RSC Adv.* 2014, 4, 676.
24. R. Kannan, A. R. Kim, K.S. Nahm, H. K. Lee, D. J. Yoo, **Chem. Comm.** 2014, 50, 14623.
25. M. A. Scibioh, S. K. Kim, E. A. Cho, T. H. Lim, S. A. Hong, H. Y. Ha, *Appl Catal B: Environ.* 2008, 84, 773.
26. R. Kannan, K. Karunakaran, S. Vasanthkumar, *J. New Mat. Elect. Syst.* 2012, 15, 249.
27. C.T, Campbell, *Nat. Chem.* 2012, 4, 2012, 597–598.
28. K.H. Ye, S. A. Zhou, X. C. Zhu, C. W. Xu, P. K. Shen, *Electrochim Acta* 2013, 90, 108.
29. V. Tripkovic, I. Cerri, T. Nagami, T. Bligaard, J. Rossmeisl, *Phys. Chem. Chem. Phys.* 2013, 15, 3279.−3285.
30. V.T. T. Ho, K.C. Pillai, H. L. Chou, C. J. Pan, J. Rick, W. N. Su, B. J. Hwang, J.F. Lee, H. S. Sheu, W. T. Chuang, *Energy Environ. Sci.* 2011, 4, 4194−4200.
31. R. Kou, Y. Shao, D. Mei, Z. Nie, D. Wang, C. Wang, V.V. Viswanathan, S. Park, I. A, Aksay, Y. Lin, Y. Wang, J. Liu, *J. Am. Chem. Soc.* 2011, 133, 2541.
32. S. Yu, Q. Liu, W. Yang, K. Han, Z. Wang, H. Zhu, *Electrochim. Acta* 2014, 94, 245.
33. H. Huang, Y. Liu, Q. Gao, W. Ruan, X. Lin, S. Li, *ACS Appl. Mater. Interfaces* 2014, 6, 10258–10264.
34. J. Paier, C. Penschke, J. Sauer, *Chem. Rev.* 2013, 113, 3949.
35. T. Masuda, H. Fukumitsu, K. Fugane, H. Togasaki, D. Matsumura, K. Tamura, Y. Nishihanta, H. Yashikawa, K. Kobayashi, T. Mori, K. Uosaki, *J. Phys. Chem. C* 2012, 116, 10098.
36. S. Aranifard, S. C. Ammal, A. Heyden, *J. Phys. Chem. C* 2014, 118, 6314.
37. M. Maidhily, T. Toyokazu, L. Peng, U. Shigenori, V. R. Gubbala, K. Rajesh, H. Junjie, H. Toru, D. Arivuoli, I . Shinsuke, A. Katsuhiko, Y. Jinhua, U. Naoto, A. Hideki, *ACS Appl. Mater. Interface* 2014, 6, 3790.
38. D. Zhang, C. Zhang, Y. Chen, Q. Wang, L. Bian, J. Miao, *Electrochim. Acta* 2014, 139, 42.
39. S. Chauhan, G. J. Richards, T. Mori, P. Yan, P. Hill, K. Ariga, K. J. Zhu, J. Drennan, *J. Mater. Chem. A* 2013, 1, 6262.
40. B. J. Li, H. Q. Cao, J. Shao, M. Z. Qu, *Chem. Commun.*, 2011, 47, 10374.
41. D. J. Xue, S. Xin, Y. Yan, K. C. Jiang, Y. X. Yin, Y. G. Guo, L. J. Wan, *J. Am. Chem. Soc.,* 2012, 134, 2512.
42. Y.-F. Han, D. Kumar, C. Sivadinarayana, *Catal. Lett.* 2004, 94, 131.
43. G. Beamson, D. Briggs, High resolution XPS of organic polymers- the scienta ESCA 300 database, Wiley Interscience, 1992, appendices 3.1 and 3.2
44. C. Zhang, J. Lin, *Phys. Chem. Chem. Phys.* 2011, 13, 3896
45. F. Vindigni, M. Manzoli, A. Damin, T. Tabakova, A. Zecchina, *Chem. Eur. J.* 2011, 17, 4356.
46. S. Stankovich, D. A. Dikin, R. D. Piner, K. A. Kohlhaas, A. Kleinhammes, Y. Jia, Y. Wu, S. T. Nguyen, R. S. Ruoff, *Carbon,* 2007, 45, 1558.